



**HAL**  
open science

## External force attached binding focus of particles and its application

Du-Chang Xu, Xiao-Ying Tang, Ao Li, Jing-Tao Ma, Yuan-Qing Xu

► **To cite this version:**

Du-Chang Xu, Xiao-Ying Tang, Ao Li, Jing-Tao Ma, Yuan-Qing Xu. External force attached binding focus of particles and its application. *Physics of Fluids*, 2023, 35 (1), 10.1063/5.0131077. hal-04544043

**HAL Id: hal-04544043**





**<https://hal.science/hal-04544043>**

Submitted on 12 Apr 2024

**HAL** is a multi-disciplinary open access archive for the deposit and dissemination of scientific research documents, whether they are published or not. The documents may come from teaching and research institutions in France or abroad, or from public or private research centers.

L'archive ouverte pluridisciplinaire **HAL**, est destinée au dépôt et à la diffusion de documents scientifiques de niveau recherche, publiés ou non, émanant des établissements d'enseignement et de recherche français ou étrangers, des laboratoires publics ou privés.

# External force attached binding focus of particles and its application

Du-Chang Xu (许都昌),<sup>1</sup>  Xiao-Ying Tang (唐晓英),<sup>1</sup> Ao Li (李澳),<sup>1</sup>  Jing-Tao Ma (马景涛),<sup>2</sup>   
and Yuan-Qing Xu (徐远清)<sup>1,a)</sup> 

## AFFILIATIONS

<sup>1</sup>School of Life Science, Beijing Institute of Technology, Zhongguancun South Street, Beijing 100081, China

<sup>2</sup>Aix Marseille Univ, CNRS, Centrale Marseille, M2P2 UMR 7340, Marseille 13451, France

<sup>a)</sup> Author to whom correspondence should be addressed: [bitxyq@bit.edu.cn](mailto:bitxyq@bit.edu.cn)

## ABSTRACT

The particle focus in the channel flow refers to a randomly initialized particle finally running at an equilibrium position at the channel cross section. The binding focus is a particle focus phenomenon that comprises two adjacent particles (including one rigid and the other soft), where particles can form and share a new equilibrium position. In this study, the result suggests that migrating the rigid particle laterally can lead to a passive migration of the soft. The above phenomenon is termed external force attached binding focus (EFABF). The EFABF is modeled to be three-dimensional using the immersed boundary-lattice Boltzmann method. The inertial focus of a single particle and the binding focus of two particles are numerically confirmed to validate the model. The migrating conditions of the soft particle are mainly discussed to further investigate the conditions of EFABF. Two patterns to migrate the soft particle are observed, including rigid particle ahead and soft particle ahead. The Reynolds number of 10 is proposed, which can apply to EFABF to obtain a significant migration scope. Moreover, the mechanism of EFABF is further analyzed to gain more insight into EFABF. Finally, as its application, a label-free single-cell separation architecture is designed by replacing the soft particle with a spherical circulating tumor cell and magnetically manipulating the rigid particle. The numerical results suggest that the soft particle (cell) can be well driven to stride over streamlines and form a new equilibrium position by migrating the rigid particle, thus making the separation pathway well-controlled.

## I. INTRODUCTION

Particle manipulation refers to a prerequisite for numerous applications based on the microfluidic chip (e.g., transportation, separation, trapping, and enrichment of particles or cells<sup>1</sup>). An appropriate particle manipulation method takes on a critical significance to bioanalysis, disease diagnostics,<sup>2</sup> and drug delivery. Over the past few years, the microfluidic methods of particle manipulation have primarily involved the following aspects: (I) acoustic tweezers:<sup>3</sup> The interference between waves reflected back and forth by the reflection and matching layer leads to the formation of standing waves and establishes a pressure distribution in the fluid. In general, solid particles and most cells gather at the pressure nodes. This method is capable of manipulating particles, cells, and organisms across different lengths, from nanometers to millimeters. (II) Dielectrophoresis (DEP): Non-charged dielectric particles are subjected to a dielectric force in a non-uniform electric field. Under this force, particles move toward or away from the stronger electric field. DEP has been extensively used for particles or cell trapping with high flexibility.<sup>4</sup> (III) Optical tweezer:<sup>5</sup> A highly focused laser

beam is capable of dragging an object with a higher refractive index than the medium to the middle of the laser beam. This method to manipulate biological single-cells exhibits high precision and noninvasive characteristic.<sup>6</sup> (IV) Magnetic manipulation<sup>7</sup> is using permanent magnets or electromagnets to manipulate cells. This method requires the surface label of cells, thus damaging cells. (V) Hydrodynamic manipulation:<sup>8</sup> Four typical methods exist for hydrodynamic manipulation: pinched flow fractionation (PFF), deterministic lateral displacement (DLD), vortex-based method, and inertial focus method (IFM).

The hydrodynamic method of particle (cell) manipulation has received extensive interest over the past few years for its advantages of high throughput and relatively simple peripheral devices.<sup>9</sup> The inertial focus method (IFM), a typical hydrodynamic manipulation, has aroused wide attention since it can achieve high-throughput particle separation of different sizes with a simple channel structure. In 1961, Segre and Silberberg established a Poiseuille flow in a circular tube, and the result indicated that neutrally buoyant finite-sized particles in pipe flow migrated toward an annulus at nearly 0.6 times the radius of

the tube,<sup>10</sup> which is termed inertial migration or inertial focus. Later research has suggested that inertial focus can arise from the competition between two effects. One effect is the shear gradient-induced lift force that pushes particles to the wall. The other effect is the wall-induced repulsive force that drives particles toward the center of the channel.<sup>11</sup>

As microfluidic technology has been leaping forward, the principle and application of inertial focus have been studied intensely in recent years. The inertial focus phenomenon provides wide possibilities for cell manipulation (e.g., transportation, separation, trapping, and enrichment<sup>12</sup>). It has aroused wide attention in biomedical and environmental research.<sup>13</sup> Labeling free detection of circulating tumor cells (CTCs) based on IFM<sup>14</sup> takes on a great significance to early stage cancer screening, diagnosis, and prognosis.<sup>15</sup> Spiral inertial microfluidics separates cells in accordance with the principle of Dean-coupled inertial migration. It has become a superior separation technology with high throughput in biomedical applications and clinical diagnosis.<sup>16</sup> The high-throughput biopsy sperm rapid separation device using a spiral channel can achieve 95.6% sperm recovery<sup>17</sup> since the sperm have different focusing positions compared with other particles. By combining inertial focus with immunomagnetic separation, the integrated biochip is capable of enriching CTC significantly, thus contributing to cancer analysis and diagnosis.<sup>18</sup>

From the perspective of inertial focus theoretical research, three aspects are summarized as follows:

The first aspect refers to the focusing characteristics of spherical particles. Shichi *et al.*<sup>19</sup> examined the inertial migration of neutrally buoyant spherical particles in square channel flows by setting the Reynolds numbers ( $Re$ ) from 1 to 800. Their result indicated that there were several specific equilibrium positions in the particle focusing, which comprised of the channel corner equilibrium position (CCE), the channel face equilibrium (CFE) position, and the intermediate equilibrium position (IME) close to the critical Reynolds number. Moreover, it is reported that the equilibrium position pattern is primarily dependent on the size ratio of the particle diameter compared with the channel width. Wang *et al.*<sup>20</sup> numerically studied the hydrodynamic behavior of small particles in the laminar channel flow. They combined with the experimental data of Matas *et al.*<sup>21</sup> for verification, and the result suggested that the equilibrium position moved to the channel center with the decrease in  $Re$ , or with the increase in the particle diameter.

The second aspect is non-spherical or elastic particle focusing characteristics. Lashgari *et al.*<sup>22</sup> numerically studied the entire migration process of flat particles in square and rectangular channels. They noted that the equilibrium position of oblate particles in the same shape with the larger rotating diameter tended to stay on the diagonal symmetry line. Connolly *et al.*<sup>23</sup> examined the inertial focus position of cancer cells with different elasticity moduli in the circular channel. Their results revealed that decreased elastic modulus made the equilibrium position closer to the channel center.

The third refers to the phenomenon and mechanism of the particle interaction in inertial focus. Schaaf *et al.*<sup>24</sup> numerically studied the inertial migration of a pair of rigid particles in the rectangular channel using the lattice Boltzmann method (LBM). The result suggested that the lift force on the leading particle was different from the lagging. Aouane *et al.*<sup>25</sup> numerically simulated the soft particle pairing mechanism induced by hydromechanics. The result revealed that they

attracted each other and formed stable pairs under weak constraints when the initial distance between two vesicles was lower than a particular value.

Extensive research on the inertial focus of multiple particles in the channel flow has suggested an interaction phenomenon between a pair of rigid and soft particles similar in size recently, termed as the binding focus state (BFS).<sup>26</sup> In the above phenomenon, particles running in the channel flow can result in inertial focus, thus exerting hydrodynamic effects on each other to change their original equilibrium positions. To be specific, when the rigid and soft particles are close in a particular scope at a specific Reynolds number, they will change their original running ways to build a new equilibrium position. This phenomenon is similar to an attraction between particles, which leads to a relatively stable combination of the two particles. In BFS, the other will be affected if one particle migrates in the lateral direction. The lateral migration of the rigid particle will produce some lateral migration on the soft. This phenomenon is defined as “external force attached binding focus” (EFABF). Inspired by this definition, this study develops a new hydrodynamic particle manipulation method, which is described as follows. The soft particle is a flexible spherical cell, and the rigid can respond to the magnetic field. The two particles are set in BFS. Subsequently, a magnetic field can be applied to migrate the rigid particle laterally across the streamline to drive the soft particle to generate an expected lateral migration.

In this study, the three-dimensional (3D) BFS and EFABF models are built with the immersed boundary-lattice Boltzmann method (IB-LBM). The lattice Boltzmann method has aroused much attention and has significantly progressed over the past decades.<sup>27,28</sup> Combined with the immersed boundary method, IB-LBM has become effective in solving problems involving fluid–structure interactions (FSIs).<sup>29–34</sup> To establish EFABF, a magnetic field perpendicular is applied to the wall surface for rigid particle manipulation to migrate the soft particle. In this study, the particle’s relative diameter, Reynolds number, and deformation characteristics of the soft particle are considered to analyze the operating conditions. To verify the theatrical deduction, a single-cell separation model is further designed in accordance with the theoretical results, and the envisaged cell separation results are successfully achieved.

This study is organized as follows. In Sec. II, the model is set. In Sec. III, the correctness of the model is verified. In Sec. IV, EFABF is introduced. In Sec. V, the EFABF model is built. In Sec. VI, the factors for EFABF are discussed in detail. In Sec. VII, the mechanism of EFABF is investigated. In Sec. VIII, a single-cell separation scheme is designed based on EFABF. Finally, the final summary is presented in Sec. IX.

## II. MATHEMATICAL MODELING

### A. Problem statement and governing equations

A 3D square microchannel is adopted to conduct the EFABF model. The channel profile with a flow velocity distribution is illustrated in Fig. 1.

As depicted in Fig. 1, the X-direction is the flow direction. Particles are set to move along with a theatrically infinite-length channel. To save computational cost, a specified length channel is employed as the flow domain, and the flow runs periodically in it. The channel is 400  $\mu\text{m}$  long ( $L$  in Fig. 1). Such a length is sufficient to avoid unphysical effects exerted by the periodic boundaries. The channel

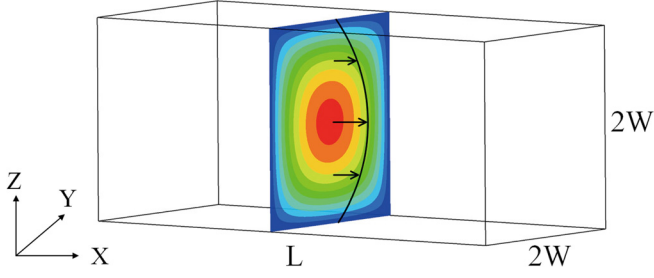


FIG. 1. Square channel and the velocity distribution on the cross section.

width (Y-direction) and height (Z-direction) are  $2W$  ( $W = 60 \mu\text{m}$ ) in size. A uniform external force  $f_{ax}$  is used to drive the fluid in the positive X direction to generate a stable Poiseuille flow. The flow is governed by the continuous Navier–Stokes equations, which is written as

$$\nabla \cdot \mathbf{u} = 0, \quad (1)$$

$$\rho \left( \frac{\partial \mathbf{u}}{\partial t} + \mathbf{u} \cdot \nabla \mathbf{u} \right) + \nabla p = \mu \nabla^2 \mathbf{u} + \mathbf{f}, \quad (2)$$

where  $\mathbf{u}$  denotes the fluid velocity,  $\rho$  is the fluid density,  $p$  is the pressure,  $\mu$  expresses the dynamic viscosity, and  $\mathbf{f}$  represents the body force.

## B. Generation of the particle surface mesh

In this study, a capsule structure is used to construct particles.<sup>35,36</sup> The corresponding unstructured grid and its construction strategy are presented in Fig. 2. To build the mesh grid, a regular icosahedron is set as the base [Fig. 2(a)]. The uniformly distributed 12 vertexes keep a given distance  $R$  from the 3D geometry's center point (marked with O). Subsequently, the midpoints on all edges of the respective triangle are taken to subdivide the original triangle into four sub-triangles [Fig. 2(b)]. It is defined as the subdividing step. Next, all the vertexes are extended in the radial direction to keep the distance  $R$  from point O, thus ensuring that all vertexes can be located on one spherical surface, which is defined as the smoothing step. Finally, to obtain the grid mesh [Fig. 2(d)], the subdividing and smoothing steps are repeated alternately until the maximum distance of neighboring grid nodes is not more than 1 ( $\Delta s < 1$ ). This operation generates 2562 nodes and 5120 triangular elements for the final grid mesh.

### 1. Mechanical description of the rigid particle

The movement of the rigid particle in a fluid can be decomposed as translation and rotation. The translational force  $F_{tra}$  and angular force  $F_{ang}$  based on the corresponding velocities are expressed as follows:<sup>37</sup>

$$\mathbf{F}_{tra} = m_p \frac{d\mathbf{U}_p}{dt} = - \int_{CS} \boldsymbol{\sigma} \cdot \mathbf{n} dS + (\rho_p - \rho_f) V_p \mathbf{g} \quad (3)$$

and

$$\mathbf{F}_{ang} = I_p \frac{d\boldsymbol{\Omega}_p}{dt} = - \int_{CS} (\mathbf{X}_s - \mathbf{X}_c) \times (\boldsymbol{\sigma} \cdot \mathbf{n}) dS. \quad (4)$$

The parameters are listed in the Nomenclature.

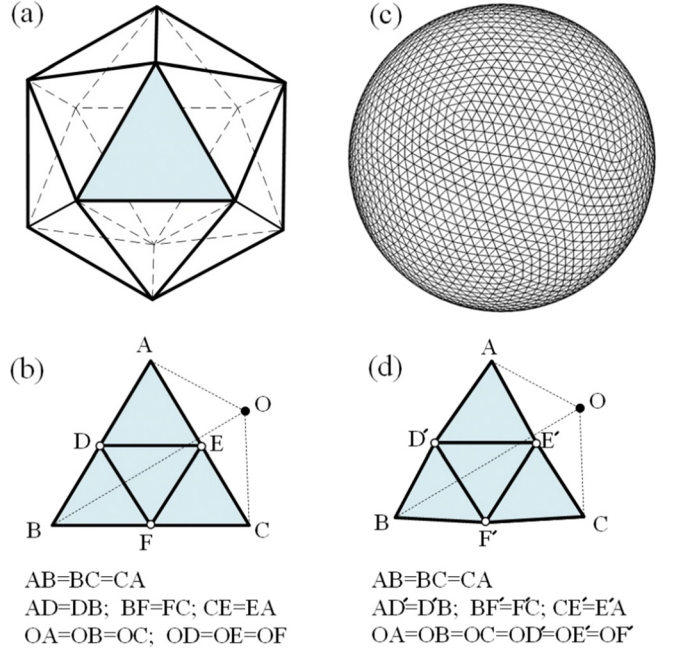


FIG. 2. Construction of the mesh grid (point O is the center of the 3D geometry): (a) the regular icosahedron base, (b) subdivision of one triangle face, (c) the final spherical mesh grid, and (d) smooth the polyhedron after subdivision.

### 2. Mechanical description of the soft particle

Unlike the rigid particle, the soft particle is flexible and will deform in the shear flow. In the inertial focus state, the particle configuration based on flexibility significantly affects the equilibrium position. To quantify the deformability of the soft particle, the Laplacian number  $La$  is introduced, which is a dimensionless number to quantify the rigidity of the soft particle. The equations for calculating  $La$  are given as follows:<sup>38</sup>

$$Re_p = Re \left( \frac{r}{W} \right)^2, \quad (5)$$

$$Re = \frac{2W u_{ave}}{\nu_f}, \quad (6)$$

$$La = \frac{Re_p}{Ca} = \frac{2k_s r}{\rho \nu_f^2}, \quad (7)$$

where  $r$  denotes the particle radius,  $u_{ave}$  represents the average fluid velocity,  $\nu_f$  expresses the fluid viscosity,  $k_s$  is the modulus governing shear deformation, and  $Ca$  denotes the capillary number, which is also a dimensionless parameter indicating the effect of surface tension on liquid flow. It can be obtained by<sup>39</sup>

$$Ca = \frac{\rho \nu_f u_{ave} r}{W k_s}. \quad (8)$$

For the soft particle in the flow, the stress and deformation are governed by the strain energy, the bending energy, and the volume conservation energy. The strain energy function due to the stretching deformation is expressed as

$$E_s = \int_{A_0} dA \left[ \frac{k_s}{12} (I_1^2 + 2I_1 - 2I_2) + \frac{k_a}{12} I_2^2 \right], \quad (9)$$

where  $E_s$  denotes the total strain energy,  $A_0$  is the surface area, and  $k_a$  is the elastic modulus for area dilation due to the conservation of surface area.  $I_1$  and  $I_2$  represent the strain invariants of the surface deformation, and they are calculated with the principal in-plane stretch ratios  $\lambda_1$  and  $\lambda_2$  as follows:

$$I_1 = \lambda_1^2 + \lambda_2^2 - 2 \quad (10)$$

and

$$I_2 = \lambda_1^2 \lambda_2^2 - 1. \quad (11)$$

To avoid the buckling of the particle surface, the bending resistance is included, and the discrete bending energy is computed as

$$E_b = \sqrt{3}k_b \sum_{\langle ij \rangle} \left[ 1 - \cos(\theta_{ij} - \theta_{ij}^0) \right], \quad (12)$$

where  $E_b$  denotes the total bending energy,  $k_b$  represents the bending modulus, and  $\theta_{ij}$  is the angle between the normal vector of two neighboring triangles.  $\theta_{ij}^0$  expresses the reference angle, which is equal to  $\theta_{ij}$  for the particle in the unstressed state.

To maintain the volume of the particle, a volume conservation energy is introduced as<sup>40</sup>

$$E_v = \frac{k_v (V - V^0)^2}{2V^0}, \quad (13)$$

where  $k_v$  is the elastic bulk modulus,  $V$  is the volume of the particle, and  $V^0$  is the reference volume of the particle in the unstressed state. In this study, a sufficiently large  $k_v$  is used to prevent volume loss, which is expressed as<sup>40</sup>

$$k_v = k_{tr} \frac{\rho \nu_f^2}{L^2}, \quad (14)$$

where  $k_{tr} = 300\,000$ . This parameter setting can make the volume change rate of the soft particle less than 1% under all flow shears involved in this study.

Finally, the resultant force  $F_L$  can be obtained by taking the derivative of total energy, which is defined as

$$\mathbf{F}_L = - \frac{\partial(E_s + E_b + E_v)}{\partial \mathbf{X}}. \quad (15)$$

### C. The IB-LBM work-frame

The IB-LBM<sup>41–45</sup> can implement deformable boundaries and simulate the interaction between particles and the flow field. In this study, the Reynolds number is located in the range of  $10^0$ – $10^2$ . In such a case, the 3D lattice Boltzmann method with the single-relaxation-time (SRT) model is adopted to solve the flow. The corresponding probability density evolution equation is expressed as<sup>46,47</sup>

$$f_i(\mathbf{x} + \mathbf{c}_i \Delta t, t + \Delta t) - f_i(\mathbf{x}, t) = -\frac{1}{\tau} [f_i(\mathbf{x}, t) - f_i^{eq}(\mathbf{x}, t)] + G_i(\mathbf{x}, t) \Delta t, \quad (16)$$

where  $f_i(\mathbf{x}, t)$  denotes the density distribution function at position  $\mathbf{x}$  and time  $t$ ,  $\mathbf{c}_i$  represents the discrete velocity,  $\Delta t$  is the time step,  $\tau$  expresses the nondimensional relaxation time,  $G_i(\mathbf{x}, t)$  is the body force term, and  $f_i^{eq}(\mathbf{x}, t)$  is the equilibrium distribution function.

The D3Q19 grid model<sup>48</sup> is used for the micro velocity description, and the corresponding discrete velocities  $\mathbf{c}_i$  is, respectively, expressed as<sup>49,50</sup>

$$(\mathbf{c}_i, i = 0, \dots, 18) = \begin{pmatrix} \mathbf{c}_{ix} \\ \mathbf{c}_{iy} \\ \mathbf{c}_{iz} \end{pmatrix} = c \begin{pmatrix} 0 & 1 & -1 & 0 & 0 & 0 & 0 & 1 & -1 & 1 & -1 & 1 & -1 & 1 & -1 & 0 & 0 & 0 & 0 \\ 0 & 0 & 0 & 1 & -1 & 0 & 0 & 1 & -1 & -1 & 1 & 0 & 0 & 0 & 0 & 1 & -1 & 1 & -1 \\ 0 & 0 & 0 & 0 & 0 & 1 & -1 & 0 & 0 & 0 & 1 & -1 & -1 & 1 & 1 & -1 & -1 & 1 & 1 \end{pmatrix}. \quad (17)$$

The equilibrium distribution function  $f_i^{eq}(\mathbf{x}, t)$  and the force term  $G_i(\mathbf{x}, t)$  are calculated by<sup>51,52</sup>

$$f_i^{eq} = \omega_i \rho \left[ 1 + \frac{\mathbf{c}_i \cdot \mathbf{u}}{c_s^2} + \frac{(\mathbf{c}_i \cdot \mathbf{u})^2}{2c_s^4} - \frac{\mathbf{u}^2}{2c_s^2} \right] \quad (18)$$

and

$$G_i(\mathbf{x}, t) = \left( 1 - \frac{1}{2\tau} \right) \omega_i \left[ \frac{\mathbf{c}_i - \mathbf{u}}{c_s^2} + \frac{\mathbf{c}_i \cdot \mathbf{u}}{c_s^4} \mathbf{c}_i \right] \cdot \mathbf{f}_p, \quad (19)$$

where  $\omega_i$  is the weight coefficient,  $c_s = \Delta x / \sqrt{3} \Delta t$  is the lattice sound speed, and  $\mathbf{f}_p$  is the body force acting on the fluid. For  $\omega_i$ , it is expressed by  $\omega_0$

relaxation time  $\tau$  is related to the kinematic viscosity  $\nu$  in Navier–Stokes equations, and it can be computed with<sup>51</sup>

$$\tau = \frac{\nu}{c_s^2 \Delta t} + 0.5. \quad (20)$$

The macroscopic fluid density, velocity, and pressure can be obtained by<sup>50,52</sup>

$$\rho = \sum_i f_i, \quad (21)$$

$$\mathbf{u} = \frac{1}{\rho} \left( \sum_i \mathbf{e}_i f_i + 0.5 \mathbf{f}_p \Delta t \right), \quad (22)$$

and

$$P = \sum_i \rho c_s^2. \quad (23)$$

The immersed boundary method is capable of exchanging information between fluid and particle surface nodes in the flow field, which is summarized as follows. On the one hand, the fluid nodes can receive the force generated by the nearby immersed boundary, and such a force will change the local flow. On the other hand, the around flow provides the motion attributes for the immersed boundary to update its position. A deformation of the immersed boundary may occur during the position change, thus leading to a recovery force. Subsequently, the fluid–structure interaction framework comes into being by repeating the above process.

The force on the particle nodes can be transferred to the surrounding fluid nodes in the following method:<sup>52</sup>

$$\mathbf{f}(\mathbf{x}, t) = \int_s \mathbf{F}_L(s, t) D[\mathbf{x} - \mathbf{X}(s, t)] ds, \quad (24)$$

where  $\mathbf{f}(\mathbf{x}, t)$  denotes the force density on the fluid nodes,  $\mathbf{F}_L(s, t)$  expresses the force density on the moving boundary nodes, and  $D[\mathbf{x} - \mathbf{X}(s, t)]$  represents the smoothed approximation of the Dirac delta function.<sup>35</sup> It is written as

$$D(\mathbf{x}) = \frac{1}{h^3} d\left(\frac{x-X}{h}\right) d\left(\frac{y-Y}{h}\right) d\left(\frac{z-Z}{h}\right), \quad (25)$$

where  $h$  denotes the grid spacing;  $d(r)$  is expressed as<sup>35</sup>

$$d(r) = \begin{cases} \frac{1}{8} (3 - 2|r| + \sqrt{1 + 4|r| - 4r^2}), & |r| \leq 1, \\ \frac{1}{8} (5 - 2|r| - \sqrt{-7 + 12|r| - 4r^2}), & 1 \leq |r| \leq 2, \\ 0, & 2 \leq |r|. \end{cases} \quad (26)$$

For the structure with the rigid particle, the force  $\mathbf{F}_L$  is determined by<sup>35</sup>

$$\mathbf{F}_L = \alpha \frac{\mathbf{U} - \mathbf{u}_{IB}}{\Delta t}, \quad (27)$$

where  $\mathbf{U}$  denotes the structural velocity obtained by solving the structure dynamics,  $\Delta t$  represents the time step, and  $\alpha$  is a positive constant;  $\mathbf{u}_{IB}$  is the interpolated velocity from the local fluid nodes, which is written as<sup>35</sup>

$$\mathbf{u}_{IB} = \int \mathbf{u}(\mathbf{x}, t) D[\mathbf{x} - \mathbf{X}(s, t)] d\mathbf{x}. \quad (28)$$

For the soft particle, the positions of the particle nodes are first updated by<sup>35</sup>

$$\frac{\partial \mathbf{X}(s, t)}{\partial t} = \mathbf{u}_{IB}. \quad (29)$$

Subsequently, the forces on the surface nodes can be updated.

### III. VALIDATIONS ON INERTIAL FOCUS AND BFS

In this section, the inertial focus of rigid and soft particles and the BFS is modeled to validate the fluid–structure coupling framework.

For the rigid particle, the focusing positions at several specific Reynolds numbers have been confirmed by other reports. Moreover, the focusing positions and the deforming configurations are verified compared with some other experimental and simulation results for the soft particle. Furthermore, the BFS is also checked based on the models of the rigid and soft particles. The above validations take on a great significance to the simulation of EFABF. For the convenience of the following descriptions, the parameters in simulations are set to default unless otherwise stated.

#### A. The inertial focus of a rigid particle

The 3D computational domain spans over  $[0, L]$  in  $x$ ,  $[-W, W]$  in  $y$ , and  $[-W, W]$  in  $z$  directions with  $L = 400 \mu\text{m}$  and  $W = 60 \mu\text{m}$ . The entrance and outlet are periodic boundaries, and other boundaries are “no-slip” walls. The density of the rigid particle (or the soft particle involved in the following section) is set as the same as the fluid. Thus, the particle can be treated as a weightless object in simulation.

There are several important parameters for analyzing inertial focus. The first is the focus position  $P_{eq}$ , which is defined as  $P_{eq} = d_0/W$ . To be specific,  $d_0$  denotes the vertical distance of the particle center to the middle section of the channel in an equilibrium state (Fig. 3). The second parameter is the relative particle size  $S_r$ . It is an index employed to measure the particle volume compared with the side length of the channel’s cross section.  $S_r = r_R/W$ , where  $r_R$  is the radius of the particle. In this section, three cases of  $S_r$  are set as 0.075, 0.125, and 0.175, respectively. The third parameter is the channel Reynolds number  $Re$ , which is set as 3, 0, 50, and 100 in the simulation. Once the channel size and fluid are selected, regulating  $Re$  refers to changing the flow speed. The fourth parameter is  $\Delta\phi_s$ , and it is the judgment criteria of the focusing state, which is defined as

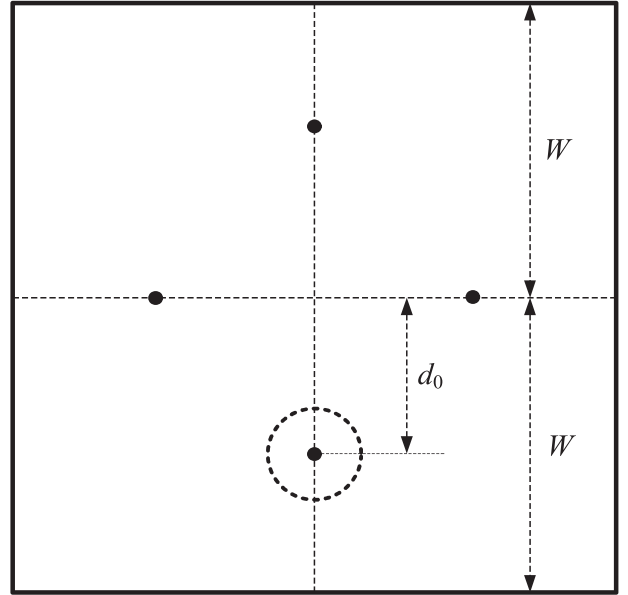


FIG. 3. The four equilibrium positions in the channel’s square cross section.

$$\Delta_{fs} = \int_t^{t+t_w} \frac{\Delta_m(t)}{W} dt \times 100\%, \quad (30)$$

where  $\Delta_m(t)$  is the lateral migration of the running particle per time step  $\Delta t$  and  $t_w$  is a time window including 1000  $\Delta t$ . Once there is  $\Delta_{fs} < 0.01\%$ , the particle reaches the focusing state.

In general, four equilibrium positions in the channel's square cross-section can be found in  $1 < Re < 100$ , as illustrated in Fig. 3. To validate the proposed model, the experimental research results of Shichi *et al.* are employed to examine the simulation results.<sup>19</sup> The results are presented in Fig. 4.

The results reveal that at  $Re = 30$  and  $50$ , the simulation results align well with the experimental results. Mark  $P_{eq}^s(Re, Sr)$  as the simulation result at a given condition of  $Re$  and  $Sr$  and  $P_{eq}^e(Re, Sr)$  as the corresponding experimental results of Shichi *et al.* Then, we know that the relative errors of  $P_{eq}$  are limited between  $\pm 0.5\%$  at  $Re = 30$  and  $50$  for all cases of  $Sr$ , where the relative errors of  $P_{eq}$  is computed by  $\frac{P_{eq}^s - P_{eq}^e}{P_{eq}^e} \times 100\%$ . This indicates that the proposed model has high accuracy at the given Reynolds numbers. Moreover, it is noted that when we increase  $Re$  to  $100$ , the relative errors of  $P_{eq}$  rise to some degree (in  $\pm 1.2\%$ ), while this is also in a relatively small range. Accordingly, the above results indicate that the proposed model is adequate for simulating the inertial focus of rigid particles.

## B. The inertial focus of a soft particle

To validate the soft particle model, the simulation results of Schaaf and Stark<sup>40</sup> are introduced to verify the simulation results, including the focusing positions and the deforming configurations in the focusing state. In accordance with Ref. 40, set  $Re = 100$  and size  $S_r = 0.2$ , and three types of Laplace numbers  $La$  are picked up as  $5$ ,  $10$ , and  $100$ . Other parameters are the same in the rigid particle case. The equilibrium positions and two deformation snapshots in the focusing state are presented in Fig. 5.

The results of Fig. 5 suggest that at different conditions, the focusing position of the soft particle may stay over the sides or at the

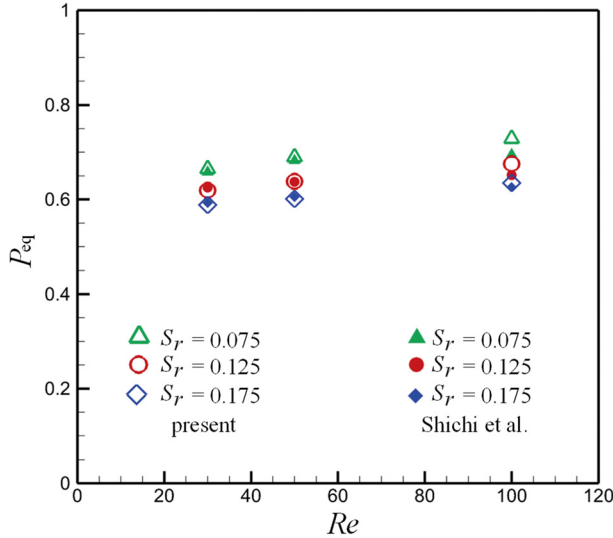


FIG. 4. Comparisons of focusing position of the rigid particles.

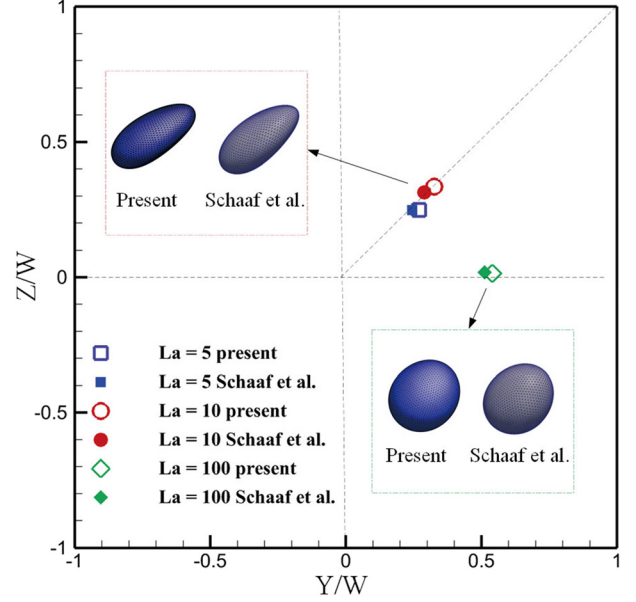


FIG. 5. The equilibrium positions and some deformation snapshots of the soft particle.

diagonal lines of the square cross section. For  $La = 100$ , the particle's equilibrium positions are located over the sides. The maximum relative error of  $P_{eq}$  reaches 2.8%. In addition, for  $La = 5$  and  $10$ , the particle runs stably at the diagonal lines of the square cross section. The maximum relative error of  $P_{eq}$  reaches 2.2% for  $La = 5$  and 3.5% for  $La = 10$ . The above analysis reveals that the proposed model is capable of predicting the same equilibrium positions in Ref. 40. Moreover, the relative errors of  $P_{eq}$  here are larger than those in the rigid particle cases, since the introduction of the deformation leads to the increased accumulated error. In addition, by comparing the deforming configurations at  $La = 10$  and  $100$ , the proposed model can obtain similar results to Ref. 40. In general, the model is feasible for simulating the inertial focus of soft particles.

## C. The BFS between the rigid and soft particles

The BFS is an interaction phenomenon between two spherical particles similar in size but different in deformability, as reported in our previous study by Li *et al.*<sup>26</sup> The research conditions of the Reynolds number are extended to further explore the principles of EFABF.

Figure 6 presents the BFS at  $Re = 10$  (with  $La = 100$  and  $S_r = 0.2$ ), which reveals that BFS can work under such a setting. Compared with the case of  $Re = 100$  in Ref. 26, the result indicates that forming BFS at  $Re = 10$  requires a longer time. As revealed by the above results, the BFS also occurs at a relatively low Reynolds number, such that BFS and EFABF are discussed in  $10 < Re < 100$ .

## IV. THE EFABF AND ITS TWO PATTERNS

In accordance with the BFS, the binding state may exist with the change of equilibrium position by applying an external force (assumed as a magnetic force marked  $F_z$  in Fig. 7) on the rigid particle. The two

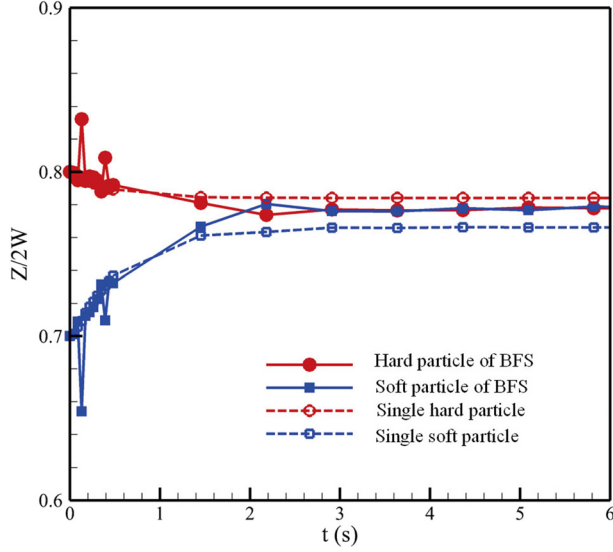


FIG. 6. Inertial focus of the single-particle case and BFS between two particles at  $Re = 10$ ,  $La = 100$ , and  $S_r = 0.2$ .

particles will migrate laterally along with the direction of  $F_z$ , which is termed EFABF. Moreover, two patterns are reported for the EFABF (Fig. 7). One is RPA (rigid particle ahead), and the other is SPA (soft particle ahead). The rigid particle is colored blue and labeled with “R,” and the soft particle is colored red and labeled with “S” in the figure to identify the particle types more conveniently.

### A. The RPA pattern

In accordance with the BFS,<sup>26</sup> the soft particle’s equilibrium position is closer to the channel center, thus resulting in a faster local flow speed around the soft particle. For the single-particle case, the soft particle runs faster than the rigid. Accordingly, the soft should be

initialized to run after the rigid to form the BFS. Otherwise, they will be apart and have no chance to interact as time passes. As a result, this is the coming of the RPA, in which the orientation of  $F_z$  is toward the wall, and the force drives the particles to approach the wall.

### B. The SPA pattern

It is assumed that the sequence of the particles in the RPA is switched, and then, the direction  $F_z$  is reversely changed, which will drive the rigid particle to approach the channel center and may run faster than the soft one. Moreover, the two particles can move close and form a new binding focus in such a case. Since the soft particle runs ahead of the rigid one, this pattern is termed “soft particle ahead” (SPA).

## V. THE CONSTRUCTION OF EFABF

### A. Setting of the channel

The channel shape takes on a critical significance to the inertial focus of particles. In some existing research, inertial focus in different channel shapes has been studied in depth.<sup>53,54</sup> Three types of channel shapes (including circular, rectangle, and square) have been commonly used. The first is the circular channel, which was first used by Segre *et al.* to report the inertial focus phenomenon. In this channel, particles in the focusing state are distributed on a ring plane perpendicular to the flow, and the equilibrium position of the particle is not fixed. In such a case, the binding focus is unstable. Thus, it does not apply to EFABF research. The second is the rectangular channel. Some research has suggested four equilibrium positions of the focusing particles over the respective edge. In addition, randomly initialized particles tend to congregate over the long edges at the end,<sup>54,55</sup> suggesting that the equilibrium positions over the long side are more stable. Moreover, the binding focus formed over the long edges is more stable, thus facilitating the establishment of EFABF. However, one disadvantage is that the particle can migrate merely in the direction of the short edges, and the lateral migration is relatively tiny in practical operations. The third refers to the square channel, with better symmetry than the rectangular channel. There are four equilibrium positions

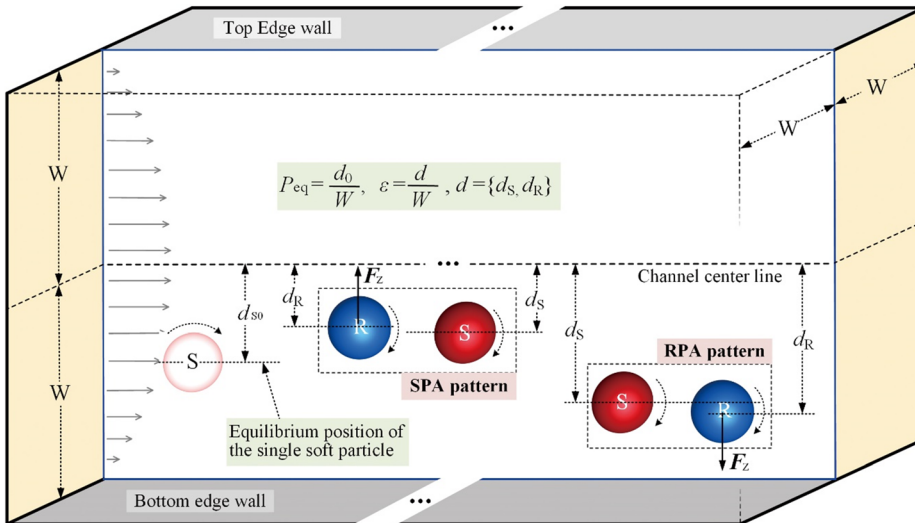


FIG. 7. The schematic diagram of EFABF and its two patterns.



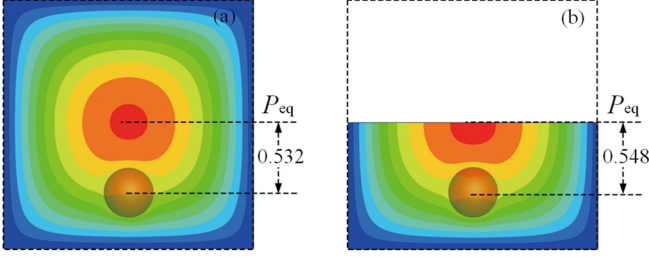


FIG. 8. Schematic diagram of particle focusing positions. The whole channel case and (b) the half channel case.

with the same stability for the focusing particle over the four edges, which can provide the stable focusing state and the migration scope of the particles. Thus, the square channel is adopted to study EFABF. Furthermore, for the square channel, an equilibrium position may exist at the channel corner at some given Reynolds number.<sup>56</sup> This study reveals that for  $Re < 100$ , such an equilibrium position exists but is easily disturbed.

## B. Setting of the time-saving computing domain

Particles running with the flow in a square channel migrate to equilibrium over one edge. Once falling into the equilibrium position, particles will always run in half the channel area. Moreover, no disturbance is identified in the flow in the other half area, suggesting that it slightly affects the particle focus. Such an effect can be ignored for the particle movement if the flow on the interface between the two half areas can be appropriately treated. Thus, a time-saving computing strategy is suggested for the study of EFABF, where only the flow in the half channel requires solving [Fig. 8(b)].

For the boundary conditions of the profile dividing the channel, the pressure and the vertical velocity are set using the extrapolation method. The horizontal velocity is a constant distribution from the fully developed channel flow.

To verify the time-saving computing domain strategy, the inertial focus of the soft particle is taken as an example. Here, set  $S_r = 0.2$ ,  $Re = 10$ , and  $La = 100$ . Contrastive results of the particle's focusing position are presented in Fig. 8, where  $P_{eq}$  in Fig. 8(b) is 0.548 and the relative error based on that (0.532) in Fig. 8(a) is nearly 3%. This error is considered to be acceptable for the study.

Moreover, with the above settings unchanged, a rigid particle ( $S_r = 0.2$ ) is added to establish the RPA pattern of BFS to conduct further verification. Moreover, three Reynolds numbers of  $Re = 5$ , 10, and 50 are considered, respectively. The results of  $P_{eq}$  are listed in Table I.

TABLE I. Comparison of  $P_{eq}$  at different  $Re$  values in the RPA pattern of BFS.

| Re | $P_{eq}$ (soft particle) |        | Relative error (%) | $P_{eq}$ (rigid particle) |        | Relative error (%) |
|----|--------------------------|--------|--------------------|---------------------------|--------|--------------------|
|    | Whole                    | Half   |                    | Whole                     | Half   |                    |
| 5  | 0.2418                   | 0.2333 | 0.85%              | 0.2153                    | 0.2079 | 0.74%              |
| 10 | 0.2340                   | 0.2247 | 0.93%              | 0.2158                    | 0.2080 | 0.78%              |
| 50 | 0.2301                   | 0.2235 | 0.66%              | 0.2053                    | 0.2017 | 0.36%              |

In the above table, “whole” and “half” represent the whole and half channel cases, respectively. Moreover, the time costs in all cases are also recorded. The results are displayed in Table II, where the computations are completed using the GPU-Cuda program. The hardware platform is Intel I7-7700k/16G/Tesla-K40C (CPU/RAM/GPU). The software is the PGI Fortran in Linux Ubuntu 20.04. The results in Table I suggest that the maximum relative error is 0.93%, less than 1%, thus revealing that the setting of the time-saving computing domain is reasonable.

Furthermore, as depicted in Table II, at least 46% of the computing time can be saved for the respective case.

## C. The control of the external force $F_z$

$F_z$  is assumed as a magnetic force acting on the rigid particle under an external magnetic field. To analyze its effect on the EFABF, a formula is written as

$$F_z = F_{z0} \left( 1 + k_t * n \left[ \frac{t}{T_w} \right] \right), \quad (31)$$

where  $F_{z0}$  denotes the initial force, which is determined by the result of making the lateral migration to be 4% of  $W$  in a single-rigid particle case at  $Re = 10$ . For the rigid particle in the SPA pattern,  $\Delta z_{R,SPA}$  is labeled as the lateral migration, and it is equal to  $|d_{R,SPA} - d_0|$ , where  $d_{R,SPA}$  denotes the distance from the rigid particle center to the channel centerline and  $d_0$  represents the initial level. Similar to the definition of  $\Delta z_{R,SPA}$ ,  $\Delta z_{R,RPA}$  expresses the lateral migration in the RPA pattern. Correspondingly, there are  $\Delta z_{S,SPA}$  and  $\Delta z_{S,RPA}$  for the soft particle. In Eq. (31),  $k_t$  denotes a constant coefficient determining the change rate of  $F_z$ , which can vary from 0.2 to 0.6. In this study,  $k_t = 0.4$ .  $n \left[ \frac{t}{T_w} \right]$  expresses a time-variant integer function, thus controlling the variation of  $F_z$ .  $T_w$  represents a presetting time window, which is long enough to switch the focusing states as  $F_z$  is changed. Here,  $n[\cdot]$  implements the rounding down operation. As a result,  $0 \leq \frac{t}{T_w} < 1$  results  $n \left[ \frac{t}{T_w} \right] = 0$ ;  $1 \leq \frac{t}{T_w} < 2$  results  $n \left[ \frac{t}{T_w} \right] = 1$ , etc. Based on  $F_z$ , the RPA and SPA patterns of EFABF can be obtained by switching the particle sequence and changing the orientation of  $F_z$ . The detailed operations are presented in Fig. 9.

In Fig. 9, the lateral migration of the particles can be expanded by increasing  $N$  from 0 up to a number  $m$ . Once beyond  $m$ , the ECABF will be broken. Subsequently, the maximum lateral migrations of the two particles can be obtained, which are expressed as  $\Delta z_{R,SPA}^m$ ,  $\Delta z_{R,RPA}^m$ ,  $\Delta z_{S,SPA}^m$ , and  $\Delta z_{S,RPA}^m$ , respectively. For the convenience of

TABLE II. Comparison of the time costs at different  $Re$  values in the RPA pattern of BFS.

| Re | Soft particle time cost (min) |      |           | Rigid particle time cost (min) |      |           |
|----|-------------------------------|------|-----------|--------------------------------|------|-----------|
|    | Whole                         | Half | Ratio (%) | Whole                          | Half | Ratio (%) |
| 5  | 863                           | 460  | 53.30%    | 867                            | 462  | 53.29%    |
| 10 | 480                           | 256  | 53.33%    | 482                            | 257  | 53.31%    |
| 50 | 287                           | 154  | 53.67%    | 288                            | 154  | 53.47%    |

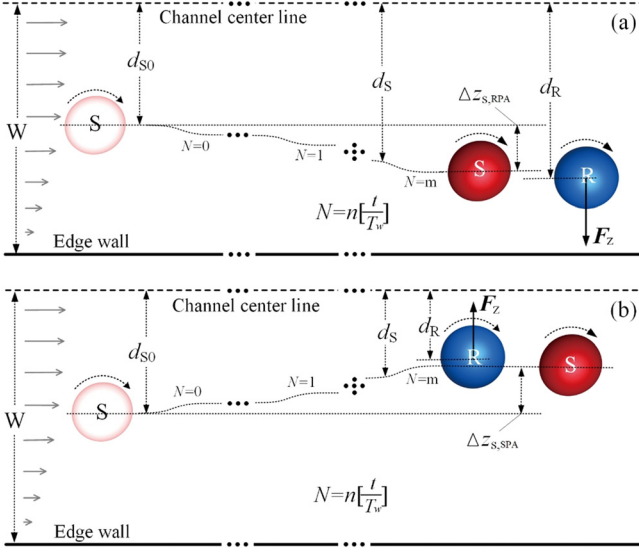


FIG. 9. Sketch maps of RPA and SPA patterns at  $F_z$ : (a) RPA pattern and (b) SPA pattern.

expressing the lateral migration range, a variable is introduced as  $\varepsilon = d/W$ . Here,  $d$  ( $d_R$  for the rigid particle and  $d_S$  for the soft particle) is the distance from the particle center to the channel centerline. It will increase in RPA or decrease in the SPA pattern if turning up  $F_z$  until EFABF is broken. Therefore,  $\varepsilon$  represents the total migration range relative to the half-channel width  $W$ . It is investigated in detail and plotted in Figs. 10–12. According to the definition of  $\varepsilon$ , we know that there must be  $(d_0 - \Delta z_{R,SPA}^m)/W \leq \varepsilon \leq (d_0 + \Delta z_{R,RPA}^m)/W$  for the rigid particle and  $(d_0 - \Delta z_{S,SPA}^m)/W \leq \varepsilon \leq (d_0 + \Delta z_{S,RPA}^m)/W$  for the soft particle.

## VI. THE INFLUENCES OF $S_r$ , $Re$ AND $La$ ON EFABF

In the EFABF, an external force is applied additionally on the rigid particle based on the BFS, such that it is more complicated to predict the performances of particles. To further understand the

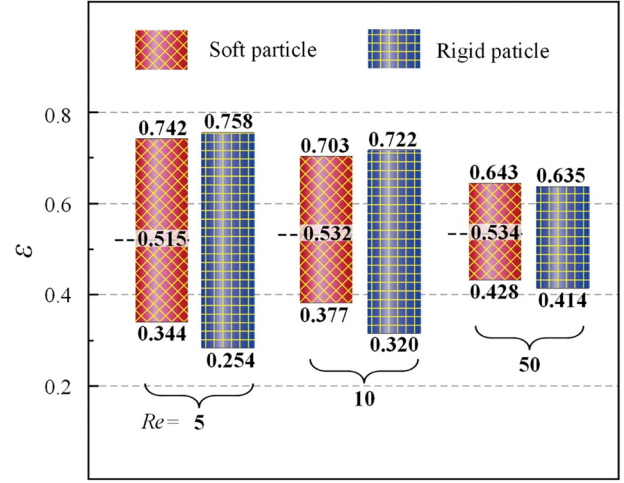


FIG. 11. Effect of  $Re$  on the lateral migration range in the EFABF.

principles of the EFABF, the particle size, deformability, and channel Reynolds number are studied individually by scanning  $F_z$  to seek the maximum lateral migration of particles. This can provide necessary reference to confirm the strength of  $F_z$  in practice.

### A. Effect of $S_r$

In this study,  $La = 100$  is set for the soft particle, and  $Re = 10$  is set to explore the effect of relative particle size  $S_r$  ( $S_r = r/W$ ) on the EFABF. To distinguish the particle types, rigid particles are marked as  $S_{rR}$ , and the soft is marked as  $S_{rS}$ . There is  $S_{rR} = S_{rS}$  in this study unless otherwise declared. Existing research has noted that the balance between the shear and the wall lift causes the inertial focus, which relates closely to the particle size. Thus, particle size is also an essential factor for the EFABF. The simulation results reveal that at a small  $S_r$  ( $<0.1$ ), the interaction between the two particles is weak, thus making the BFS less steady. External interference can easily breakup the focus state. In addition, at a large  $S_r$  ( $>0.4$ ), the balance on the focusing state

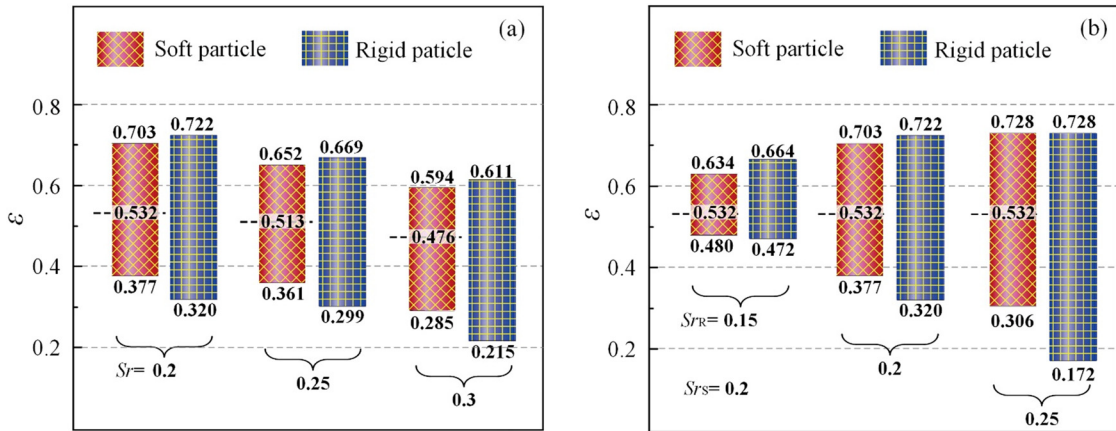


FIG. 10. Effect of the particle size on its lateral migration in the EFABF: (a)  $S_r = S_{rR} = S_{rS}$ ,  $S_r = 0.2, 0.25$ , and  $0.3$ ; and (b)  $S_{rS} = 0.2$ ,  $S_{rR} = 0.15, 0.2$ , and  $0.25$ .

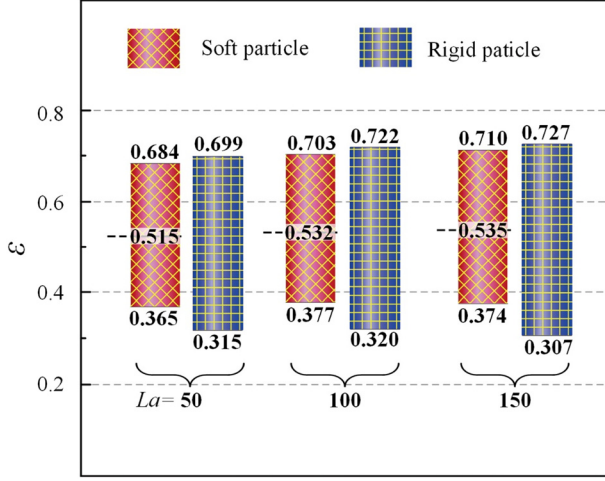


FIG. 12. Effect of  $La$  on the lateral migration range in the EFABF.

will be hard to maintain. Accordingly, in this study, we discussed the EFABF by varying  $S_r$  from 0.15 to 0.35, such a scope of particle size is appreciated to generate a relatively stable particle focusing state for the EFABF.

In this part, two cases are considered. In the first case, the soft and the rigid particles exhibit the same sizes ( $S_r = S_{rR} = S_{rS}$ ), which are set individually as 0.2, 0.25, and 0.3 to analyze the EFABF. In the second case,  $S_{rS}$  is 0.2, and  $S_{rR}$  is regulated as 0.15, 0.2, and 0.25. The corresponding lateral migration range is defined as  $\varepsilon = d/W$  by applying an external force to migrate the rigid particle laterally, where  $d = \{d_S, d_R\}$ ,  $d_S$  ( $d_R$ ) is the distance from the soft (rigid) particle center to the channel centerline.  $d_0 = \{d_{S0}, d_{R0}\}$  is the initial value.

In Fig. 10, the red square columns filled with diagonal lines express the lateral migration range of the soft particle. The height of the column is the total lateral migration range measured by  $\varepsilon$ . The value on the upper end of the column is obtained by  $(d_0 + \Delta z_{R,RPA}^m)/W$  for the rigid particle or  $(d_0 + \Delta z_{S,RPA}^m)/W$  for the rigid particle. The value below the bottom of the column is obtained by  $(d_0 - \Delta z_{R,SPA}^m)/W$  for the rigid particle or  $(d_0 - \Delta z_{S,SPA}^m)/W$  for the soft particle. The short dashed lines go through the middle part of the column marked the  $\varepsilon$  level at  $d_S = d_{S0}$  (or at  $F_z = 0$ ). Moreover, the blue squared columns filled with horizontal and vertical lines are set for the rigid particle. The first case's results are presented in Fig. 10(a). Four aspects are summarized as follows. First, in  $0.2 \leq S_r \leq 0.3$ , the extended scopes of lateral migration are similar for both particles. Second, the particle centers tend to get closer to the channel centerline by increasing the particle size. Third, for all three cases, the total lateral migration range of the rigid particle is nearly 25% larger than that of the soft particle. Fourth, by computing  $\varepsilon/S_r$ , we know that smaller particles can be migrated more evidently relative to their sizes in the EFABF. The second case's results are presented in Fig. 10(b), where  $S_{rS}$  is fixed as 0.2. It is found that increasing the rigid particle size can expand the migration scope of both particles. Moreover, compared with the RPA pattern, a more extensive lateral migration of the rigid particle is required to generate a given lateral migration for the soft particle in the SPA pattern.

## B. Effect of $Re$

Here,  $S_{rR} = S_{rS} = 0.2$  and  $La = 100$  are set.  $Re$  is set as 5, 10, and 50 by varying  $u_{ave}$  in Eq. (6), respectively, for the EFABF model, where  $u_{ave}$  is determined as

$$u_{ave} = \frac{1}{4W^2} \int_{y=-W}^{y=W} \int_{z=-W}^{z=W} u(x_c, y, z) dy dz, \quad (32)$$

where  $x_c$  denotes a constant coordinate in the flow direction.  $x_c = W$  is selected in the simulation. As mentioned above, a uniform external force  $f_{ax}$  is applied in the positive  $X$ -direction to generate the channel flow, such that the channel  $Re$  relates directly to  $f_{ax}$ . To seek the proper  $f_{ax}$  for a given  $Re$ , a feedback adjustment strategy is employed by testing the fully developed channel flow, where the practical errors of  $Re$  are allowed in  $\pm 1\%$ .

The lateral migration ranges in all cases are presented in Fig. 11. As depicted in the figure, the variation range of  $\varepsilon$  is the widest at  $Re = 5$ , and there is a decreasing trend for the range by the increasing  $Re$ . As revealed by the above result, at a relatively low  $Re$ , the particle binding is steadier, and the soft particle can be driven to produce a larger lateral migration. Thus, a relatively low Reynolds number contributes to particle binding and EFABF. However, at a relatively low  $Re$ , a longer time should reach the focusing state. Thus, given both the lateral migration range and the practical operation,  $Re = 10$  is the appreciated condition.

## C. Effect of $La$

Laplace number  $La$  refers to a measure of the deformability of the soft particle. At the same shear rate, a higher  $La$  will result in less deformation. In this section, we set  $S_{rR} = S_{rS} = 0.2$  and  $Re = 10$  as the fixed conditions.  $La = 10$  is first considered, whereas the results suggest that the BFS exhibits relatively weak stability. In other words, a small external force on the rigid particle can break the binding state. Accordingly,  $La$  is picked up as 50, 100, and 150 for the model. Figure 12 presents the results of  $\varepsilon$  under the three cases of  $La$ .

The total lateral migration range of the soft (rigid) particle are 0.319 (0.384), 0.326 (0.402), and 0.336 (0.420) for  $La = 50, 100,$  and  $150$ , respectively. The results indicate that the lateral migration ranges of the two particles will be expanded slightly with the rising of  $La$ . Moreover, the expansion of the rigid particle is slightly larger than the soft. In general, for all three settings of  $La$ , the level changes of  $\varepsilon$  are not remarkable, whereas there is a clear variation trend. According to the simulation results, the deformation cases of the soft particles under three  $La$  are similar, which may explain why no significant changes of  $\varepsilon$  are observed.

## VII. THE MECHANISM ANALYSIS ON EFABF

In Sec. VI, the effects of  $S_r$ ,  $Re$ , and  $La$  on the EFABF are discussed, where the principles of the particles' lateral migration are mainly investigated. In this section, by comparing with the BFS, the physical mechanisms of EFABF are analyzed. Here,  $S_{rR} = S_{rS} = 0.2$ ,  $Re = 10$  and  $La = 100$  are set for all cases. The particle positions and the pressure distributions are presented in Fig. 13. In which, the pressure is nondimensionalized by  $c_s^2(\rho - \rho_0)/(\rho_0 U_0^{*2})$ . (In LBM,  $\rho_0 = 1$  is the reference density;  $U_0^* = 0.0105$  is the reference velocity, which is obtained from the channel centerline at  $Re = 10$ ).

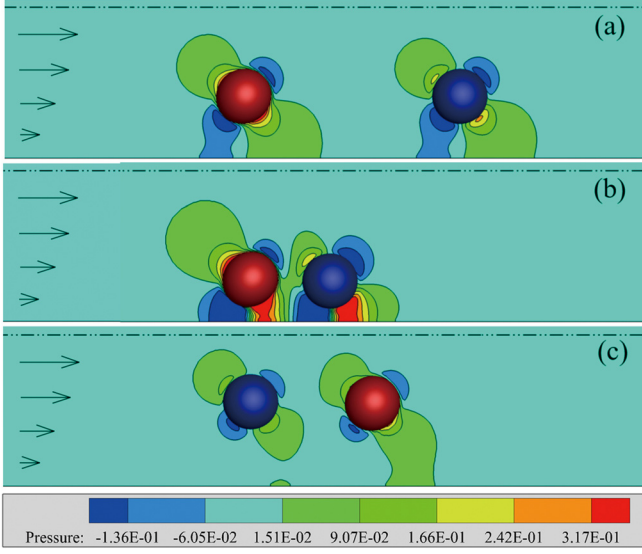


FIG. 13. The particle positions and the pressure distributions of the flow field. (a) BFS; (b) EFABF-RPA; and (c) EFABF-SPA.

In Fig. 13, case (a) originates from BFS, case (b) is from EFABF-RPA, and case (c) originates from EFABF-SPA. Two aspects are analyzed in the following.

The first aspect is the particle position. For the horizontal particle positions, (a) has the largest particle–particle distance, followed by (c), and (b) has the smallest distance. For the focus positions ( $P_{eq}$ ), the cases follow an order of (b), (a), and (c) from large to small. It is known that the particle–particle distance is essentially determined by  $P_{eq}$ . The case of  $S_r = 0.2$  in Fig. 10 indicates that the maximum  $\varepsilon$  of the soft is smaller than that of the rigid, suggesting that the soft will be closer to the channel centerline in (b) compared with (a). Subsequently, the soft obtains a relatively higher speed to pursue its former rigid particle, thus making the two particles closer in (b). Likewise, (c) indicates that the minimum  $\varepsilon$  of the soft is larger than that of the rigid, suggesting that the rigid will be closer to the channel centerline in (c) compared with (a). Next, the rigid obtains a relatively higher speed to pursue its former soft particle, which also makes the two particles closer. Furthermore, different shear rates at their focus positions make the particle–particle distance in (c) more extensive than that in (b). As revealed by the above result, under the same external force level, the change of  $P_{eq}$  ( $\Delta P_{eq}$ ) is also different. Here,  $|F_z| = 2.848 \times 10^{-3}$  [ $F_z$  is nondimensionalized by  $F_z^*/(\rho U_0^2 D_R^2)$ ,  $F_z^* = 1.8084 \times 10^{-4}$  is the driving force in LBM.  $D_R = 24$  is the diameter of the rigid particle at  $S_R = 0.2$ ], and  $\Delta P_{eq}(\text{soft})$  reaches 0.142 in (b) and 0.112 in (c).

The second aspect is the changes in the pressure distributions. (a) is taken as the reference. The variation range of pressure in (b) is enlarged whereas it decreases in (c). For case (b),  $F_z$  points to the wall, thus magnifying the “shear lift” toward the wall to form a new focus state, where a much larger “wall lift” toward the channel centerline should hold the mechanical balance. This finding explains the significantly enhanced positive pressure between the wall and the particles. A similar analysis also applies to the explanation of the pressure reduction in (c).

Next, the particles’ motion principles in BFS and EFABF are discussed. The nondimensional velocity of the flow field is expressed as  $(UX, UY, UZ)$ . The velocity at the rigid particle center is expressed as  $(UX_{R_c}, UY_{R_c}, UZ_{R_c})$ .  $UX0 = UX - UX_{R_c}$  is set, and then, the colormap of  $UX0$  and the streamlines of  $(UX0, UY, UZ)$  are presented in Fig. 14.

Four points can be summarized as follows. First, it is found the particle rotation directions in all three cases are clockwise. The above results are reasonable since  $UX$  at the upper part is always larger than the below part, which will result in a clockwise torque on the particle. Second, the nondimensional horizontal velocity of the rigid particle center  $U_R$  ( $U_R = U_{R_c}^*/U_0^*$ , where \* denotes the LBM work frame) is recorded, which are 0.6952, 0.4752, and 0.8505 from (a) to (c). These results indicate a smaller  $P_{eq}$  corresponds to a higher horizontal velocity of the particle. Third, the nondimensional rotational angular rates of the rigid particle  $\omega_{R,\theta}$  [ $\omega_{R,\theta} = \omega_{R,\theta}^*/(U_0^*/D_R)$ ] are also computed, which are 0.0336, 0.0215, and 0.0400 from (a) to (c). Thus, a smaller  $P_{eq}$  corresponds to a smaller rotational angular velocity of the particle. Fourth, the shear rate is significantly larger when approaching the wall, such that the soft particle in (b) deforms more distinguishably compared with (a) and (c).

## VIII. SIMULATION STUDY OF CELL MANIPULATION BASED ON EFABF

Single-cell analysis often requires cell migration in the fluid, where the cell should be picked up first and then sent to a specified position. For example, the circulating tumor cell analysis for early diagnosis of cancer metastasis. In this section, a potential application scene of EFABF in cell analysis is studied, which exhibits cell manipulation in controlling its pathway.

The scheme is presented in Fig. 15. A separator (partition) is set nearly to the outlet with a thickness of  $W/12$ . The obstacle of such a thickness will not lead to an apparent disturbance to the laminar flow. In default mode [Fig. 15(a)], the cell in the focus state will pass over

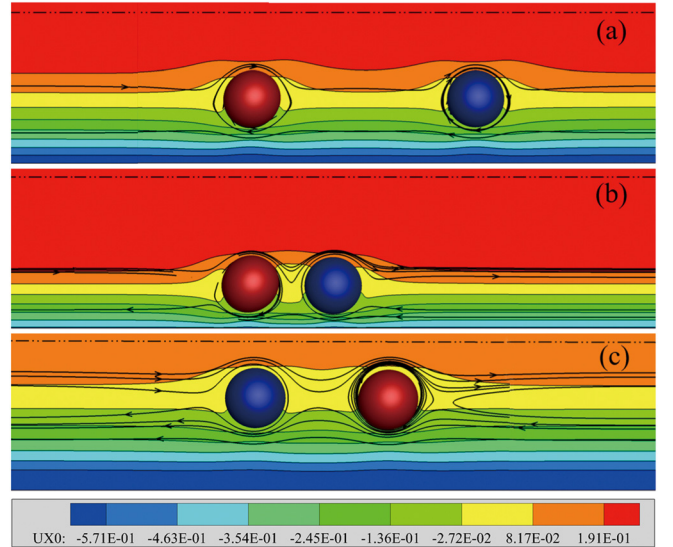
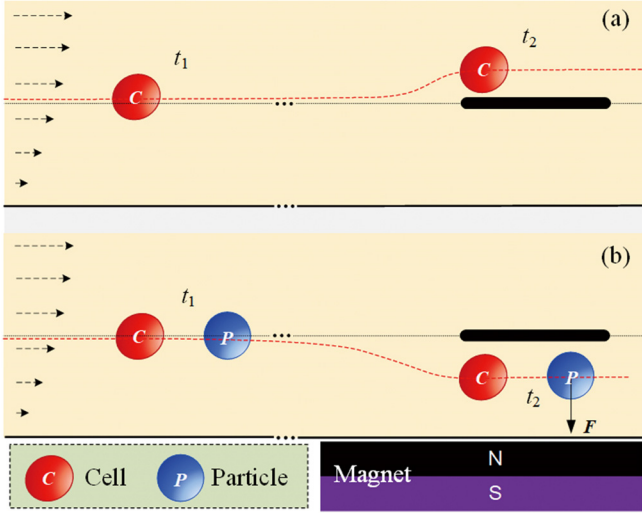


FIG. 14. The streamlines and horizontal velocity colormap by fixing the rigid particle center: (a) BFS, (b) EFABF-RPA, and (c) EFABF-SPA.



**FIG. 15.** The design scheme of cell manipulation system based on EFABF principle. (a) Single-cell case; and (b) EFABF-based cell manipulation.

the separator. In contrast, in the controlling mode [Fig. 15(b)], the cell will move down with the particle under the magnet force and pass below the separator by applying the EFABF-RPA pattern. The above result reveals that the magnet can control the motion of the cell according to the EFABF principle.

A 3D model is built based on Fig. 15. Here we set  $Re = 10$ ,  $S_{rg} = S_{rs} = 0.2$ , and  $La = 100$  for the model. The half-square channel is still adopted to optimize the computation, as illustrated in Fig. 8(b). The Bounce-Back principle of LBM is employed to construct the separator. Figure 16 presents the results. As depicted in Figs. 16(a)–16(c), the cell eventually passes over the separator, and (d)–(f) exhibit the process that the cell passes below the separator following the rigid particle.

The simulation results suggest that the EFABF principle applies to the control of cell motion. It is a nondestructive cell manipulation

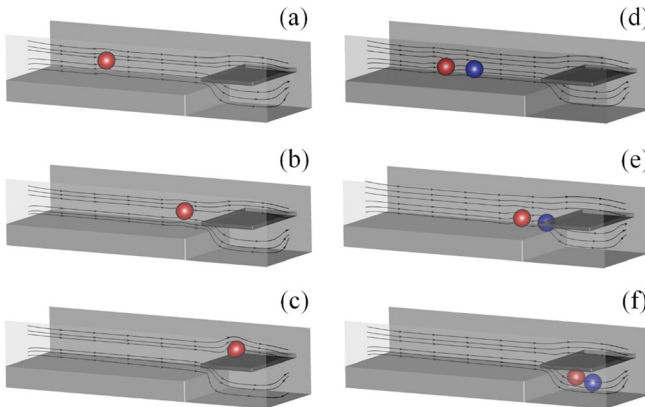


**FIG. 16.** Simulation results of cell manipulation system based on EFABF principle. (a) 0; (b) 0.02; (c) 0.04; (d) 0; (e) 0.03; and (f) 0.05 s.

method. Moreover, it is also an example to show how to use a magnetic field to control a nonmagnetic object (cell). In brief, this study reveals that EFABF has the potential to provide a type of novel cell manipulation method.

## IX. SUMMARY AND CONCLUSION REMARKS

In this study, the migration principles of the two particles in BFS are mainly studied by introducing an external force. In the study, a magnetic field perpendicular to the wall surface is set to migrate the rigid particle across streamlines and manipulate the soft particle, termed EFABF, where the effects of particle size, Reynolds number, and deformability of the soft particle are discussed in detail, and five main conclusions can be summarized below. (I) Two patterns called RPA and SPA can be established by changing the direction of the external force and switching the particle sequence. (II) To optimize the channel size and achieve a practicable lateral migration for the soft particle, the relative particle size is recommended as  $S_{rg} = S_{rs} = 0.2$ . (III)  $Re = 10$  meets both conditions of lateral migration range and operating time cost. (IV) At  $Re = 10$ ,  $La$  in the field of 50 to 150 has a similar scope of lateral migration for the particles. (V) The simulation results of single-cell sorting show that EFABF has a broad application prospect in cell manipulation.

In addition, this study has several limitations. Only the manipulation of a single soft particle is discussed. The interaction of multiple particles remains unclear. Moreover, many non-spherical cells exist in actual cases (e.g., ellipsoidal or club particles). This study cannot extend directly to the above non-spherical particles since the binding focus of these particles may be quite different from the spherical particles, which requires further study.

## ACKNOWLEDGMENTS

This study is supported by the National Natural Science Foundation of China (No. 82172066) and the Beijing Municipal Natural Science Foundation (No. Z190014).

## AUTHOR DECLARATIONS

### Conflict of Interest

The authors have no conflicts to disclose.

### Author Contributions

**Du-Chang Xu:** Data curation (lead); Formal analysis (equal); Investigation (lead); Methodology (lead); Validation (lead); Writing – original draft (equal). **Xiao-Ying Tang:** Conceptualization (equal); Formal analysis (equal); Resources (lead); Supervision (equal). **Ao Li:** Conceptualization (supporting); Data curation (supporting); Investigation (supporting); Methodology (equal); Validation (equal); Visualization (equal); Writing – original draft (supporting); Writing – review & editing (lead). **Jing-Tao Ma:** Conceptualization (supporting); Data curation (supporting); Investigation (supporting); Methodology (equal); Validation (equal); Visualization (equal); Writing – original draft (supporting); Writing – review & editing (lead). **Yuan-Qing Xu:** Conceptualization (lead); Data curation (equal); Formal analysis (lead); Funding acquisition (equal); Project administration (equal); Writing – original draft (equal); Writing – review & editing (equal).

## DATA AVAILABILITY

The data that support the findings of this study are available from the corresponding author upon reasonable request.

## NOMENCLATURE

|                         |                              |
|-------------------------|------------------------------|
| CS                      | Particle surface             |
| $\mathbf{g}$            | Gravitational acceleration   |
| $I_p$                   | Moment of inertia            |
| $\mathbf{n}$            | Normal vector                |
| $\mathbf{U}_p$          | Translational velocity       |
| $\mathbf{X}_c$          | Point of the particle center |
| $\mathbf{X}_s$          | Points on the particle       |
| $\rho_f$                | Density of fluid             |
| $\rho_p$                | Density of particle          |
| $\boldsymbol{\sigma}$   | Fluid stress tensor          |
| $\boldsymbol{\Omega}_p$ | Angular velocity             |

## REFERENCES

- 1D. Van Assche, E. Reithuber, W. Qiu, T. Laurell, B. Henriques-Normark, P. Mellroth, P. Ohlsson, and P. Augustsson, "Gradient acoustic focusing of sub-micron particles for separation of bacteria from blood lysate," *Sci. Rep.* **10**, 3670 (2020).
- 2P. Kanithamniyom and Y. Zhang, "Magnetic digital microfluidics on a bioinspired surface for point-of-care diagnostics of infectious disease," *Electrophoresis* **40**, 1178 (2019).
- 3A. Ozcelik, J. Rufo, F. Guo, Y. Gu, P. Li, J. Lata, and T. J. Huang, "Acoustic tweezers for the life sciences," *Nat. Methods* **15**, 1021 (2018).
- 4H. Sun, Y. Ren, L. Hou, Y. Tao, W. Liu, T. Jiang, and H. Jiang, "Continuous particle trapping, switching, and sorting utilizing a combination of dielectrophoresis and alternating current electrothermal flow," *Anal. Chem.* **91**, 5729 (2019).
- 5S. Kumar, M. Gunaseelan, R. Vaipully, A. Kumar, M. Ajith, G. Vaidya, S. Dutta, and B. Roy, "Pitch-rotational manipulation of single cells and particles using single-beam thermo-optical tweezers," *Biomed. Opt. Express* **11**, 3555 (2020).
- 6S. Hu, J.-y. Ye, Y. Zhao, and C.-I. Zhu, "Advanced optical tweezers on cell manipulation and analysis," *Eur. Phys. J. Plus* **137**, 1024 (2022).
- 7A. N. Surendran, R. Zhou, and Y. Lin, "Microfluidic devices for magnetic separation of biological particles: A review," *J. Med. Devices* **15**, 024001 (2021).
- 8A. Volpe, C. Gaudiuso, and A. Ancona, "Sorting of particles using inertial focusing and laminar vortex technology: A review," *Micromachines* **10**, 594 (2019).
- 9X. Xu, X. Huang, J. Sun, R. Wang, J. Yao, W. Han, M. Wei, J. Chen, J. Guo, and L. Sun, "Recent progress of inertial microfluidic-based cell separation," *Analyst* **146**, 7070 (2021).
- 10G. Segre and A. Silberberg, "Radial particle displacements in Poiseuille flow of suspensions," *Nature* **189**, 209 (1961).
- 11G. Lauricella, J. Zhou, Q. Luan, I. Papautsky, and Z. Peng, "Computational study of inertial migration of prolate particles in a straight rectangular channel," *Phys. Fluids* **34**, 082021 (2022).
- 12B. B. Fuchs, S. Eatemadpour, J. M. Martel-Foley, S. Stott, M. Toner, and E. Mylonakis, "Rapid isolation and concentration of pathogenic fungi using inertial focusing on a chip-based platform," *Front. Cell. Infect. Microbiol.* **9**, 27 (2019).
- 13N. Xiang, Q. Li, Z. Shi, C. Zhou, F. Jiang, Y. Han, and Z. Ni, "Low-cost multi-core inertial microfluidic centrifuge for high-throughput cell concentration," *Electrophoresis* **41**, 875 (2020).
- 14A. Abdulla, T. Zhang, S. Li, W. Guo, A. R. Warden, Y. Xin, N. Maboyi, J. Lou, H. Xie, and X. Ding, "Integrated microfluidic single-cell immunoblotting chip enables high-throughput isolation, enrichment and direct protein analysis of circulating tumor cells," *Microsyst. Nanoeng.* **8**, 13 (2022).
- 15Z. Habli, W. AlChamaa, R. Saab, H. Kadara, and M. L. Khraiche, "Circulating tumor cell detection technologies and clinical utility: Challenges and opportunities," *Cancers* **12**, 1930 (2020).
- 16N. Liu, C. Petchakup, H. M. Tay, K. H. H. Li, and H. W. Hou, "Spiral inertial microfluidics for cell separation and biomedical applications," in *Applications of Microfluidic Systems in Biology and Medicine*, Bioanalysis, Vol. 7 (Springer, Singapore, 2019), pp. 99–150.
- 17H. Feng, A. Jafek, R. Samuel, J. Hotaling, T. G. Jenkins, K. I. Aston, and B. K. Gale, "High efficiency rare sperm separation from biopsy samples in an inertial focusing device," *Analyst* **146**, 3368 (2021).
- 18Y. Gou, J. Liu, C. Sun, P. Wang, Z. You, and D. Ren, "Inertial-assisted immunomagnetic bioplatfrom towards efficient enrichment of circulating tumor cells," *Biosensors* **11**, 183 (2021).
- 19H. Shichi, H. Yamashita, J. Seki, T. Itano, and M. Sugihara-Seki, "Inertial migration regimes of spherical particles suspended in square tube flows," *Phys. Rev. Fluids* **2**, 044201 (2017).
- 20Q. Wang, D. Yuan, and W. Li, "Analysis of hydrodynamic mechanism on particles focusing in micro-channel flows," *Micromachines* **8**, 197 (2017).
- 21J.-P. Matas, J. F. Morris, and É. Guazzelli, "Inertial migration of rigid spherical particles in Poiseuille flow," *J. Fluid Mech.* **515**, 171 (2004).
- 22I. Lashgari, M. N. Ardekani, I. Banerjee, A. Russom, and L. Brandt, "Inertial migration of spherical and oblate particles in straight ducts," *J. Fluid Mech.* **819**, 540 (2017).
- 23S. Connolly, K. McGourty, and D. Newport, "The influence of cell elastic modulus on inertial positions in Poiseuille microflows," *Biophys. J.* **120**, 855 (2021).
- 24C. Schaaf, F. Rühle, and H. Stark, "A flowing pair of particles in inertial microfluidics," *Soft Matter* **15**, 1988 (2019).
- 25O. Aouane, A. Farutin, M. Thiébaud, A. Benyoussef, C. Wagner, and C. Misbah, "Hydrodynamic pairing of soft particles in a confined flow," *Phys. Rev. Fluids* **2**, 063102 (2017).
- 26A. Li, G.-M. Xu, J.-T. Ma, and Y.-Q. Xu, "Study on the binding focusing state of particles in inertial migration," *Appl. Math. Modell.* **97**, 1–18 (2021).
- 27Z. Chai, H. Liang, R. Du, and B. Shi, "A lattice Boltzmann model for two-phase flow in porous media," *SIAM J. Sci. Comput.* **41**, B746 (2019).
- 28B. Wen, B. Huang, Z. Qin, C. Wang, and C. Zhang, "Contact angle measurement in lattice Boltzmann method," *Comput. Math. Appl.* **76**, 1686 (2018).
- 29D. Hui, Z. Xu, W. Wu, G. Zhang, Q. Wu, and M. Liu, "Drafting, kissing, and tumbling of a pair of particles settling in non-Newtonian fluids," *Phys. Fluids* **34**, 023301 (2022).
- 30L. Zhu, X. Yu, N. Liu, Y. Cheng, and X. Lu, "A deformable plate interacting with a non-Newtonian fluid in three dimensions," *Phys. Fluids* **29**, 083101 (2017).
- 31Z.-h. Huang, Y.-g. Cheng, J.-y. Wu, W. Diao, and W.-x. Huai, "FSI simulation of dynamics of fish passing through a tubular turbine based on the immersed boundary-lattice Boltzmann coupling scheme," *J. Hydrodyn.* **34**, 135 (2022).
- 32M. Wang, Y. Feng, D. Owen, and T. Qu, "A novel algorithm of immersed moving boundary scheme for fluid-particle interactions in DEM-LBM," *Comput. Methods Appl. Mech. Eng.* **346**, 109 (2019).
- 33T. Ma, F. Qin, W. Cheng, and X. Luo, "Influence of vibrating wall on micro-swimmer migration in a channel," *Phys. Fluids* **34**, 051905 (2022).
- 34P. Zhang, S. Sun, Y. Chen, S. Galindo-Torres, and W. Cui, "Coupled material point Lattice Boltzmann method for modeling fluid-structure interactions with large deformations," *Comput. Methods Appl. Mech. Eng.* **385**, 114040 (2021).
- 35J. Ma, Z. Wang, J. Young, J. C. Lai, Y. Sui, and F.-B. Tian, "An immersed boundary-lattice Boltzmann method for fluid-structure interaction problems involving viscoelastic fluids and complex geometries," *J. Comput. Phys.* **415**, 109487 (2020).
- 36N. Takeishi, H. Yamashita, T. Omori, N. Yokoyama, and M. Sugihara-Seki, "Axial and nonaxial migration of red blood cells in a microtube," *Micromachines* **12**, 1162 (2021).
- 37Z.-G. Feng and E. E. Michaelides, "Proteus: A direct forcing method in the simulations of particulate flows," *J. Comput. Phys.* **202**, 20–51 (2005).
- 38A. H. Raffee, S. Dabiri, and A. M. Ardekani, "Elasto-inertial migration of deformable capsules in a microchannel," *Biomicrofluidics* **11**, 064113 (2017).
- 39T. Krüger, B. Kaoui, and J. Harting, "Interplay of inertia and deformability on rheological properties of a suspension of capsules," *J. Fluid Mech.* **751**, 725 (2014).
- 40C. Schaaf and H. Stark, "Inertial migration and axial control of deformable capsules," *Soft Matter* **13**, 3544 (2017).

- <sup>41</sup>F. Jiang, H. Liu, X. Chen, and T. Tsuji, "A coupled LBM-DEM method for simulating the multiphase fluid-solid interaction problem," *J. Comput. Phys.* **454**, 110963 (2022).
- <sup>42</sup>D.-K. Sun and Z. Bo, "Numerical simulation of hydrodynamic focusing of particles in straight channel flows with the immersed boundary-lattice Boltzmann method," *Int. J. Heat Mass Transfer* **80**, 139 (2015).
- <sup>43</sup>X. Zhu, S. Wang, Q. Feng, L. Zhang, L. Chen, and W. Tao, "Pore-scale numerical prediction of three-phase relative permeability in porous media using the lattice Boltzmann method," *Int. Commun. Heat Mass Transfer* **126**, 105403 (2021).
- <sup>44</sup>T. Hafemann, S. Tschisgale, and J. Frohlich, "A simulation method for particle migration in microfluidic spirals with application to small and medium particle concentrations," *Phys. Fluids* **32**, 123303 (2020).
- <sup>45</sup>J. Z. Liu, H. Liu, and Z. H. Pan, "Numerical investigation on the forming and ordering of staggered particle train in a square microchannel," *Phys. Fluids* **33**, 073301 (2021).
- <sup>46</sup>W. Liu and C.-Y. Wu, "Modelling complex particle–fluid flow with a discrete element method coupled with lattice Boltzmann methods (DEM-LBM)," *ChemEngineering* **4**, 55 (2020).
- <sup>47</sup>T. Huang and H.-C. Lim, "Simulation of lid-driven cavity flow with internal circular obstacles," *Appl. Sci.* **10**, 4583 (2020).
- <sup>48</sup>W. Wu, X. Liu, J. Liu, S. Zeng, C. Zhou, and X. Wang, "Investigation into yaw motion influence of horizontal-axis wind turbine on wake flow using LBM-LES," *Energies* **14**, 5248 (2021).
- <sup>49</sup>H. Hao, J. Yu, Y. Song, F. Chen, and T. Liu, "Deformation and regimes of liquid column during water exit of a partially submerged sphere using the front-tracking lattice Boltzmann method," *J. Fluids Struct.* **99**, 103152 (2020).
- <sup>50</sup>Y. Sui, Y.-T. Chew, P. Roy, and H.-T. Low, "A hybrid method to study flow-induced deformation of three-dimensional capsules," *J. Comput. Phys.* **227**, 6351 (2008).
- <sup>51</sup>Z. Guo, C. Zheng, and B. Shi, "Discrete lattice effects on the forcing term in the lattice Boltzmann method," *Phys. Rev. E* **65**, 046308 (2002).
- <sup>52</sup>F.-B. Tian, H. Luo, L. Zhu, J. C. Liao, and X.-Y. Lu, "An efficient immersed boundary-lattice Boltzmann method for the hydrodynamic interaction of elastic filaments," *J. Comput. Phys.* **230**, 7266 (2011).
- <sup>53</sup>J.-Y. Kwon, T. Kim, J. Kim, and Y. Cho, "Particle focusing under Newtonian and viscoelastic flow in a straight rhombic microchannel," *Micromachines* **11**, 998 (2020).
- <sup>54</sup>C. Liu, G. Hu, X. Jiang, and J. Sun, "Inertial focusing of spherical particles in rectangular microchannels over a wide range of Reynolds numbers," *Lab Chip* **15**, 1168 (2015).
- <sup>55</sup>A. A. S. Bhagat, S. S. Kuntaegowdanahalli, and I. Papautsky, "Inertial microfluidics for continuous particle filtration and extraction," *Microfluid. Nanofluid.* **7**, 217 (2009).
- <sup>56</sup>K. Miura, T. Itano, and M. Sugihara-Seki, "Inertial migration of neutrally buoyant spheres in a pressure-driven flow through square channels," *J. Fluid Mech.* **749**, 320 (2014).